

# Deep and intermediate-depth non-double couple earthquakes: interpretation of moment tensor inversions using various passbands of very broadband seismic data

Keiko Kuge<sup>1,\*</sup> and Hitoshi Kawakatsu<sup>2,\*\*</sup>

<sup>1</sup> Department of Geophysics, Faculty of Science, Kyoto University, Kyoto 606-01, Japan

<sup>2</sup> Geological Survey of Japan, Tsukuba 305, Japan

Accepted 1992 June 24. Received 1992 June 12; in original form 1991 December 10

## SUMMARY

Analysis of moment tensor inversions using various passbands of very broadband seismic data provides clear evidence that some non-double couple moment tensors of intermediate-depth and deep earthquakes result from the superposition of different double couple sources whose predominant principal axes are aligned with the predominant strain state within the subducting slabs. The analyses are performed for three intermediate-depth and deep earthquakes: 1984 January 1 south of Honshu (386 km), 1985 April 23 Luzon (181 km), and 1987 May 7 northern Sea of Japan (417 km). Consistent non-double couple moment tensors obtained using different sets of seismic waves in various low frequency bands suggest that these three significant non-double couple components are not caused by unmodelled propagation errors of seismic waves in the inversion procedure, because the various sets of seismic waves traverse very different ray paths. For the south of Honshu and the Luzon events, two major arrivals in the broadband *P*-wave displacement seismograms are observed, with varying relative amplitudes or polarities from station to station. The different double couple mechanisms which model the two phases combine to produce the significant non-double couple moment tensors obtained at long periods. The principal axes of the subevents, closest in orientation to the predominant strain states within the slabs, tend to be quite stable, whereas the other two principal axes rotate between subevents. This observation may explain the global nature of non-double couple components in relation to the strain regime within the slab. For the northern Sea of Japan event, two major phases are observed in the *P*-wave displacement waveforms, but the variation in mechanism of two subevents that we model is not enough to explain the large non-double couple component observed at long periods. However, since the non-double couple component is exceptionally large compared with those for other deep earthquakes, changes of focal mechanism with shorter delays than we can resolve appear to explain the overall radiation most simply.

**Key words:** deep earthquake, non-double couple component, mechanism change.

## 1 INTRODUCTION

Although the existence of intermediate-depth and deep earthquakes has long been recognized, the physical

\* Present address: Institute of Tectonics, University of California at Santa Cruz, Santa Cruz, CA 95064, USA.

\*\* Present address: Earthquake Research Institute, University of Tokyo, Tokyo 113, Japan.

mechanism responsible for such events is still not understood. The source mechanisms of most shallow earthquakes are well explained by brittle failure or frictional sliding of rocks. Displacement on a fault plane (i.e. shear dislocation) can be represented by a double couple source as long as the wavelengths are much larger than the source volume. At high temperatures and pressures within subducting slabs, it is not clear how brittle failure or

frictional sliding can occur. Even at high strain rates, ductile behaviour is likely, since pressure controlled by normal stresses predicts frictional strengths in excess of stresses required for ductile deformation (Frohlich 1989).

Nonetheless, it is very interesting that seismic radiation from intermediate-depth and deep earthquakes is often consistent with shear dislocation. Assuming that radiation patterns of intermediate-depth and deep earthquakes are quadrupolar, a great number of double couple focal mechanisms have been determined (e.g. Isacks & Molnar 1971). Directivity of the source duration observed in body waveforms (e.g. Mikumo 1972), the locations of subevents (e.g. Oike 1971; Fukao 1972), and the hypocentral distributions of deep events (e.g. Billington & Isacks 1975; Giardini & Woodhouse 1984) have some spatial systematics with the configuration of the nodal planes of deep events, suggesting dislocation on a fault. Furthermore, Kawakatsu (1991a) showed that the isotropic components of deep earthquakes (depth > 300 km) are small relative to the deviatoric components of the source moment tensors.

For the physical mechanisms of these deep earthquakes, many candidates have been proposed, such as brittle fracture due to high pore pressure (e.g. Griggs & Handin 1960; Raleigh & Paterson 1965), shear-induced melting (e.g. Griggs & Baker 1969), and plastic instability (e.g. Hobbs & Ord 1988). Some experimental studies under non-hydrostatic pressure suggested that phase transformations in metastable phases in rocks may be a mechanism to explain the apparent shear dislocations at great depth (e.g. Randall 1966; Sung & Burns 1976; Kirby 1987; Kirby, Durham & Stern 1991). Green & Burnley (1989) and Burnley, Green & Prior (1991) observed that a shear dislocation nucleated from the phase transformation ( $\alpha \rightarrow \gamma$ ) in  $\text{Mg}_2\text{GeO}_4$ , and proposed that an analogous process can occur to produce deep earthquakes (depth > 300 km). This mechanism is expected for the phase transformation ( $\alpha \rightarrow \beta$ ) of natural olivine (Green *et al.* 1990). For earthquakes shallower than 250–300 km, a different mechanism is necessary; for example, brittle failure assisted by pore fluid (Green & Burnley 1989; Kirby *et al.* 1991), because the olivine–spinel phase transition cannot be associated and other metastable phase transformations above 250 km are not expected. On the other hand, observations of acoustic emissions under realistic high pressure suggested that intermediate-depth and deep earthquakes may be caused by the dehydration and amorphization of hydrous minerals within slabs (Meade & Jeanloz 1991).

While the physical mechanisms have been proposed mostly in terms of shear dislocation, recent systematic study of the deviatoric parts of moment tensors suggests that some intermediate-depth and deep earthquakes show significant deviations from double couple mechanisms, or so-called 'non-double couple components' (e.g. Dziewonski & Woodhouse 1983a; Giardini 1983, 1984). This deviation from simple shear dislocation radiation is apparently related with the strain states within dipping slabs (Giardini 1983, 1984; Kuge & Kawakatsu 1992). If such non-double couple components are intrinsic in the intermediate-depth and deep sources, we should consider a specific physical mechanism for non-double couple sources (for example, change in shear modulus in the axial strain field, Knopoff & Randall 1970) as well as a physical mechanism for shear dislocation. Study

of non-double couple components is thus essential to understand the physical mechanism of intermediate-depth and deep earthquakes.

Analysis of very broadband seismic data is a very powerful way to examine non-double couple components. A deep earthquake occurred south of Honshu, Japan on 1984 January 1 (9:03:40.1 UT, 33.62°N, 136.80°E, depth = 386.0 km,  $m_b = 6.4$ , ISC) for which the Harvard centroid moment tensor (CMT) solution deviates significantly from a double couple mechanism (Ekström, Dziewonski & Steim 1986). It is often suspected that a non-double couple moment tensor is produced in the inversion by unmodelled propagation errors; for example, unmodelled heterogeneous structure along the ray paths (Solomon & Julian 1974), unmodelled velocity structure and time corrections at each station (Doornbos 1985), or lack of appropriate station coverage (Satake 1985). For the non-double couple moment tensor of the south of Honshu deep event, however, this is not the case. Kuge & Kawakatsu (1990) studied the non-double couple moment tensor using very broadband data. The non-double couple moment tensors separately obtained using different seismic waves at different frequency bands are consistent with each other. If unmodelled propagation errors were responsible for the significant non-double couple moment tensor, such consistent solutions are unlikely because seismic waves traversing different paths were used in each inversion. The non-double couple moment tensor estimated at long periods is produced by the superposition of different double couple sources which model several phases in the broadband *P*-wave displacement waveforms with amplitude ratios that vary from station to station. The large non-double couple component of this event is very likely to be a manifestation of the presence of subevents with different double couple mechanisms in a single rupture sequence.

Changes in focal mechanism and combinations of different focal mechanisms have been proposed to explain the non-double couple components of deep earthquakes (e.g. Dziewonski & Woodhouse 1983a; Giardini 1984; Frohlich 1989; Frohlich, Riedesel & Apperson 1989) because different focal mechanisms of the subevents have already been pointed out for several deep events (e.g. Strelitz 1980; Choy & Boatwright 1981). On the other hand, there has been no evidence for deep and intermediate-depth events that the existence of observed subevents can really explain the non-double couple component estimated using long-period seismograms, although this has been suggested for shallow earthquakes (Ekström & Dziewonski 1985; Kikuchi, Kanamori & Satake 1992). Some combinations of different double couples cannot produce any non-double couple components (e.g. double-couples with the same direction of the null axis). Such analyses as Kuge & Kawakatsu (1990) are necessary.

In this study, we analyse two additional non-double couple earthquakes, the 1985 April 23 Luzon earthquake (16:15:11.0 UT, 15.32°N, 120.63°E, depth = 181 km,  $m_b = 6.3$ , ISC) and the 1987 May 7 northern Sea of Japan earthquake (03:05:48.2 UT, 46.75°N, 139.22°E, depth = 417 km,  $m_b = 5.9$ , ISC), using very broadband data. These two events are selected for the following reasons. (1) This type of analysis requires good station coverage and high quality broadband data. Both events have exceptionally

good station coverage by the recent digital network; (2) the broadband *P*-wave displacement records from both events show the presence of several distinct subevents which are well isolated in time. These events should complement the south of Honshu event for studying the origins of non-double couple earthquakes.

We assume in this study that the isotropic part of moment tensor is zero, and only the deviatoric parts are examined. We use the same definition as Giardini (1983, 1984) for a non-double couple component as follows,

$$\varepsilon = -\frac{\lambda_2}{\max(|\lambda_1|, |\lambda_3|)} \quad (1)$$

where  $\lambda_i$  represents an eigenvalue of the deviatoric part of moment tensor ( $\lambda_1 \geq \lambda_2 \geq \lambda_3$ ). The parameter  $\varepsilon$  is zero in the case of a double couple source, and  $\pm 0.5$  in the case of CLVD sources (Knopoff & Randall 1970).

**Table 1.** Data of very broadband waveform analysis for the 1985 April 23 Luzon event (depth = 181 km, ISC).

SRO	$\phi$	$\Delta$	CMT surface	CMT body	LP P&SH	BB
ASRO						
ANMO	41	113	○	○	x	x
CHTO	283	21	t	○	x	x
CTAO	144	43	x	z	○	○
GRFO	322	90	○	h	x	x
GUMO	91	24	h	○	x	x
MAJO	33	26	○	○	x	x
NWAO	184	48	○	○	P	○
SNZO	141	75	○	○	○	○
ZOBO	98	172	z	○	x	x
DWWSSN						
BDF	266	169	h	○	x	x
COL	26	77	x	○	○	○
GAC	13	117	○	○	x	x
GDH	358	95	○	○	x	x
HON	71	77	z	○	○	○
JAS	45	102	x	○	x	x
SLR	246	99	○	○	x	x
TAU	158	63	○	○	○	○
TOL	319	105	h	h	x	x
RSTN						
RSNY	12	119	○	○	x	x
RSON	22	107	○	○	x	x
RSSD	32	108	○	○	x	x
NARS						
NE02	329	89	x	x	x	○
IDA						
ALE	0	82	z	x	x	x
BDF	266	169	z	x	x	x
CMO	26	77	z	x	x	x
ERM	31	33	z	x	x	x
ESK	332	95	z	x	x	x
GUA	91	24	z	x	x	x
KIP	71	77	z	x	x	x
KMY	303	19	z	x	x	x
NNA	81	163	z	x	x	x
PFO	47	107	z	x	x	x
RAR	113	86	z	x	x	x
SJG	12	146	z	x	x	x
SUR	240	106	z	x	x	x
WWSSN						
KOD	269	42	x	x	x	○

$\phi$  and  $\Delta$  represent azimuth (degree) from the north and epicentral distance (degree), respectively. Circles show the data used, whereas crosses show no data used. Labels 'z', 'h', and 't' represent only a vertical, a horizontal and a transverse component, respectively. Labels 'P' represent only *P*-waves to be modelled.

## 2 VERY BROADBAND WAVEFORM ANALYSIS

We retrieve source moment tensor representations using waveforms with four different frequency bands; the centroid moment tensor (CMT) inversions for the surface waves (3 ~ 10 mHz) and for the long-period body waves (12 ~ 20 mHz), the inversion of *P* and *SH* waveforms from GDSN long-period channels (~0.04 Hz), and the broadband *P*-wave displacement waveform analysis (0.02 ~ 1.0 Hz). Note that we independently estimate moment tensor solutions by performing each waveform inversion separately. Tables 1 and 2 list the data. The analysis mainly consists of two parts: the long-period and broadband waveform analyses.

We consider two kinds of effects of unmodelled structure on moment tensors: one is the effect of errors in the propagation of seismic waves by unmodelled local structure along seismic rays, and the other is the effect of unmodelled near-source structure whose scale is less than the wave lengths used in our analyses and whose effect could be

**Table 2.** Data of very broadband waveform analysis for the 1987 May 7 northern Sea of Japan event (depth = 417 km, ISC).

SRO	$\phi$	$\Delta$	CMT surface	CMT body	LP P&SH	BB
ASRO						
ANMO	49	80	○	○	P	○
ANTO	309	71	○	○	P	x
BCAO	276	107	○	○	x	x
CHTO	243	43	○	○	○	○
CTAO	173	67	○	○	○	○
GUMO	170	33	x	x	P	x
KONO	335	66	○	○	○	○
MAJO	211	10	○	○	x	x
NWAO	198	82	○	○	○	○
SNZO	154	93	○	○	x	x
TATO	219	26	x	○	x	x
ZOBO	46	142	z	z	x	x
DWWSSN						
BDF	347	149	z	○	x	x
CMB	56	70	○	○	○	○
COL	37	42	○	○	○	○
GAC	337	83	○	○	x	x
GDH	355	64	○	○	○	○
HON	94	56	○	○	○	x
KEV	337	54	○	○	SH	○
LEM	217	60	x	○	SH	x
LON	49	63	○	○	○	○
SCP	27	87	○	○	SH	○
SLR	265	122	○	○	x	x
TAU	174	90	x	x	SH	x
TOL	333	88	x	x	SH	○
IDA						
ALE	356	51	z	x	x	x
CMO	323	70	z	x	x	x
GUA	169	33	z	x	x	x
KMY	246	36	z	x	x	x
NNA	307	134	z	x	x	x
PFO	303	75	z	x	x	x
SJG	334	112	z	x	x	x
HAL	344	87	z	x	x	x
WWSSN						
HKC	228	63	x	x	x	○
KOD	256	63	x	x	x	○
NDI	272	51	x	x	x	○
POO	265	60	x	x	x	○

$\phi$  and  $\Delta$  represent azimuth (degree) from the north and epicentral distance (degree), respectively. Circles show the data used, whereas crosses show no data used. Labels 'z' represent only a vertical component. Labels 'P' and 'SH' represent only *P*- and *SH*-waves to be modelled, respectively.

common for the radiations of different seismic waves. We estimate the former effect (unmodelled propagation error effect) in this analysis by comparing moment tensor solutions obtained using different seismic waves traversing different paths. On the other hand, we cannot assess the latter effect (unmodelled near-source structure effect) even by comparing those moment tensor solutions in the different inversions. These effects are thus discussed later, especially in connection with the non-double couple component of the northern Sea of Japan event.

## 2.1 Long-period waveform analysis

### 2.1.1 CMT inversion

We analyse surface waves and long-period body waves separately using the CMT inversion program written locally by Kawakatsu (1989). In a CMT inversion, both the hypocentral location and moment tensor solution are determined using normal modes of the earth. The inversion method is described in Dziewonski, Chou & Woodhouse (1981) and Dziewonski & Woodhouse (1983a, b). To compute normal modes, we use earth model 1066a (Gilbert & Dziewonski 1975) and the  $Q^{-1}$  model of Masters & Gilbert (1983). Data are from long-period channels of GDSN and IDA stations. We mainly model surface wavetrains coming along minor arcs, band-pass filtered between 3.5 to 7.0 mHz for the Luzon event, and 4.5 to 10.0 mHz for the northern Sea of Japan event. We use the higher frequency bands for the northern Sea of Japan event because the event is smaller. For the long-period body waves, we use the wavetrains from  $P$  arrivals to just before Love wave arrivals, band-pass filtered between 12 and 20 mHz.

### 2.1.2 Inversion of $P$ and $SH$ waveforms from GDSN long-period channels

We estimate moment tensors using  $P$  and  $SH$  waveforms from GDSN long-period channels by an inversion scheme based on ray theory. We use GDSN long-period seismograms for which the peak frequency of the narrowband instrument response is around 40 mHz.  $P$  waves and shorter-period ( $>20$  mHz)  $SH$  waves are almost completely neglected in CMT inversions. The parameterization of the inversion closely follows Nábělek (1984). The source time function and moment tensor are simultaneously estimated in the inversion, whereas source location is not explicitly included in the inversion procedure. We use a source time function described as a sum of symmetric triangles whose half duration is 2 s. Change of the half duration has little effect on our results. Geometrical spreading factors and ray parameters are computed for the isotropic PREM Earth model (1 Hz) (Dziewonski & Anderson 1981). Time alignment for seismograms is obtained by maximizing the correlation coefficient between synthetic and observed waveforms. We use the inverse of the power of observed seismograms at each station as weighting factors to give equal weights to all seismograms.

For the northern Sea of Japan event, we use only the direct  $P$  and  $SH$  waves. The time lengths of the waveforms for  $P$  and  $SH$  waves are 45 and 50 s, respectively. For the

Luzon event, we model  $P$  wavetrains 120 s long, which include the direct wave and the depth phases (i.e.  $pP$  and  $sP$  waves), as well as the direct  $SH$  waves. For the latter event, the waveforms of the  $P$ -waves depend on the source depth. After performing inversions at several source depths, we choose a moment tensor solution at the depth (170 km) which minimizes the total variance from the observed waveforms.

## 2.2 Broadband waveform analysis

We determine focal mechanism solutions (moment tensor or double couple) for subevents of each rupture using broadband  $P$ -wave displacement seismograms. The data are deconvolved from GDSN long-period and short-period records following Harvey & Choy (1982), or from GDSN intermediate-period records. The waveforms are band-pass filtered between about 0.02 and 1.0 Hz. As we will show later, two major phases are observed in the seismograms from all three events considered. We estimate the focal mechanism solutions of two subevents for each earthquake.

By measuring the difference in time between the arrivals from the two subevents, we determine the relative time and location of the second subevent by the directivity analysis. We then obtain the focal mechanisms by an iterative focal mechanism inversion for the two subevents. We first determine only the focal mechanism and source time function of the first subevent using the beginning parts of the waveforms. The focal mechanism and source time function of the second subevent are then estimated by modelling the observed waveforms from which the synthetic waveforms of the first subevent have been subtracted. The inversion scheme is the same as the inversion of  $P$  and  $SH$  waveforms from GDSN long-period channels. Details of the procedure and parameters are presented in the following sections for each event.

## 2.3 Error estimates for moment tensors

For the covariance matrix, we use a degree of freedom in the frequency domain instead of a degree of freedom in the time domain (i.e. the number of data points) because the real degree of freedom of the data should be less than the number of the data points when the data are bandpass-filtered.

We describe a degree of freedom for the  $i$ th seismogram as follows,

$$\text{frd}_i = \text{frd}_0 \frac{N_i}{N_{\text{FFT}}}, \quad (2)$$

where  $N_i$  and  $N_{\text{FFT}}$  are the number of the data points and the number of points used for the FFT procedure, respectively.  $\text{frd}_0$  corresponds to the number of the points in the frequency domain which can pass through a filter. It should be  $N_{\text{FFT}}$  if all the frequency band is used. The total degree of freedom for  $n$  seismograms is

$$\text{FRD} = \sum_n \text{frd}_i - n_{\text{par}}, \quad (3)$$

where  $n_{\text{par}}$  is the number of parameters in the inversion. We scale the covariance matrix by FRD. Our error estimates are

several times larger than those obtained from the total number of data points.

### 3 THE 1985 APRIL 23 LUZON EARTHQUAKE

The three solutions on the left side of Fig. 1 and Table 3 are the results of the long-period waveform analysis. These solutions are very similar to each other and show significant deviations from a double couple source. The non-double couple component  $\epsilon$  is estimated to be  $0.23 \pm 0.07$  from these solutions. The Harvard CMT solution obtained using a different velocity model from ours is also consistent with these solutions and has a large non-double couple component ( $\epsilon = +0.17$ ) (Dziewonski, Franzen & Woodhouse 1986). The fact that different seismic waves are used in each inversion with different frequency bands, spatial distributions, and noise properties indicates that the source itself, or unmodelled near-source structure effect, is responsible for the significant non-double couple component observed consistently in the long-period waveform analyses. This is also confirmed by the variation of non-double couple components of other events beneath Luzon (Figs 2a and b).

The *P*-wave broadband displacement waveforms at NE02, NWA0, COL and TAU are shown in Fig. 3. Two major phases are seen in the waveforms. The second phase arrives around 10 s after the initial motion of the first phase. The moment tensor solution shown in Fig. 3 is obtained from the CMT inversion using long-period body waves (Fig. 1 and Table 3). We can clearly see the change in polarity between the two subevents at stations located near the nodal plane. The waveform at COL shows the same polarities of the initial motions for the two subevents, whereas the waveform at TAU has different polarities, i.e. compression for the first phase and dilatation for the second phase (see arrows in Fig. 3).

We estimate the relative origin time and location of the second subevent by the directivity analysis (Fig. 4). Arrival times of the first ( $t_1$ ) and the second ( $t_2$ ) subevents are read in each broadband displacement waveform. We use seven

**Table 3.** Moment tensor solutions in the very broadband analysis of the 1985 April 23 Luzon event (depth = 181 km, ISC).

	CMT surface	CMT body	GDSN LP	BB
$M_0$	2.539	1.947	2.39	1.892
$M_{xx}$	$2.564 \pm 0.073$	$2.471 \pm 0.246$	$2.500 \pm 0.242$	$1.844 \pm 0.097$
$M_{yy}$	$-1.042 \pm 0.067$	$-0.965 \pm 0.216$	$-0.680 \pm 0.208$	$-0.622 \pm 0.095$
$M_{zz}$	$-1.523 \pm 0.044$	$-1.505 \pm 0.169$	$-1.831 \pm 0.185$	$-1.222 \pm 0.054$
$M_{xy}$	$0.690 \pm 0.052$	$0.113 \pm 0.127$	$0.178 \pm 0.126$	$0.278 \pm 0.131$
$M_{yz}$	$-0.905 \pm 0.037$	$-0.752 \pm 0.059$	$-0.781 \pm 0.060$	$-0.780 \pm 0.045$
$M_{zx}$	$0.650 \pm 0.029$	$0.793 \pm 0.100$	$0.783 \pm 0.010$	$0.565 \pm 0.048$
$\epsilon$	$0.21 \pm 0.02$	$0.30 \pm 0.03$	$0.17 \pm 0.06$	0.14

The moment tensor solution labelled 'BB' is the sum of the two double couple sources:  $62.4/76.8/-135.9$  (strike/dip/slip[degree]) ( $M = 1.23$ ) and  $84.9/51.5/-91.4$  ( $M = 0.86$ ). Unit of  $M_0$  and  $M_{ij}$  is  $\times 10^{19}$  Nm. The error ranges of  $\epsilon$  are estimated in the first-order approximation (equation 6).

*P*-wave displacement waveforms at GDSN stations, and one WWSSN station (KOD) to supplement station coverage to the west. If two subevents occur at different locations, the difference in time between the phase arrivals from the two subevents ( $\Delta t = t_2 - t_1$ ) should be a function of the azimuths and take-off angles of the seismic waves to the stations. Using  $\Delta t_{\text{obs}}$ , we estimate the relative origin time ( $\tau$ ) and location of the second subevent. The location is represented by the distance ( $\gamma$ ), dip angle ( $\delta$ ), and azimuth ( $\phi$ ) from the first subevent. For given  $\tau$ ,  $\gamma$ ,  $\delta$ , and  $\phi$ , we can compute the predicted time difference between the phase arrivals from the two subevents ( $\Delta t_{\text{predict}}^{(i)}$ ) for each station, and the sum of the squared residuals between the observed and predicted time difference, which is,

$$V = \sum_i (\Delta t_{\text{obs}}^{(i)} - \Delta t_{\text{predict}}^{(i)})^2 \quad (4)$$

where the superscript 'i' corresponds to the *i*th station.

We use a two-step procedure to determine  $\tau$ ,  $\gamma$ ,  $\delta$ , and  $\phi$ . In the first step, we estimate  $\tau$  and  $\gamma$  for a given pair of  $\delta$  and  $\phi$ , using  $\Delta t_{\text{predict}}^{(i)} = \gamma \cos \theta_i / V_p + \tau$ , where  $V_p$  is the *P*-wave velocity around the source, and  $\theta$  is the angle

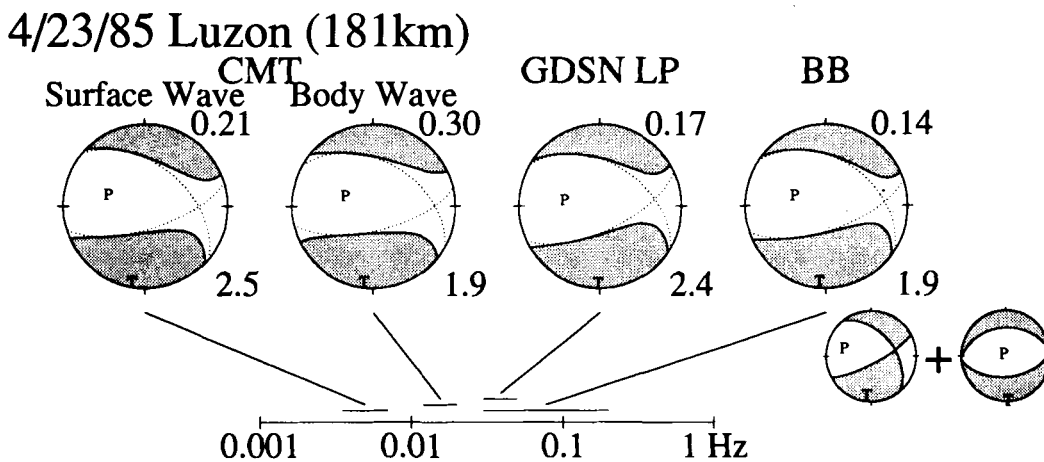


**Figure 1.** Comparison of the moment tensor solutions obtained at four different frequency bands in the very broadband waveform analysis for the 1985 April 23 Luzon event (depth = 181 km, ISC). Numbers at the upper-right and lower-right side of each solution represent the non-double couple component ( $\epsilon$ ) and seismic moment ( $\times 10^{19}$  Nm), respectively. The focal mechanisms are shown on lower hemisphere projections.

between the directions to a station along the seismic ray and to the location of the second subevent, both measured from the location of the first subevent. Fig. 4a shows  $\Delta t_{\text{obs}}^{(i)}$  (open circles) and  $\Delta t_{\text{predict}}$  (a solid line). We estimate  $\gamma$  and  $\tau$  from

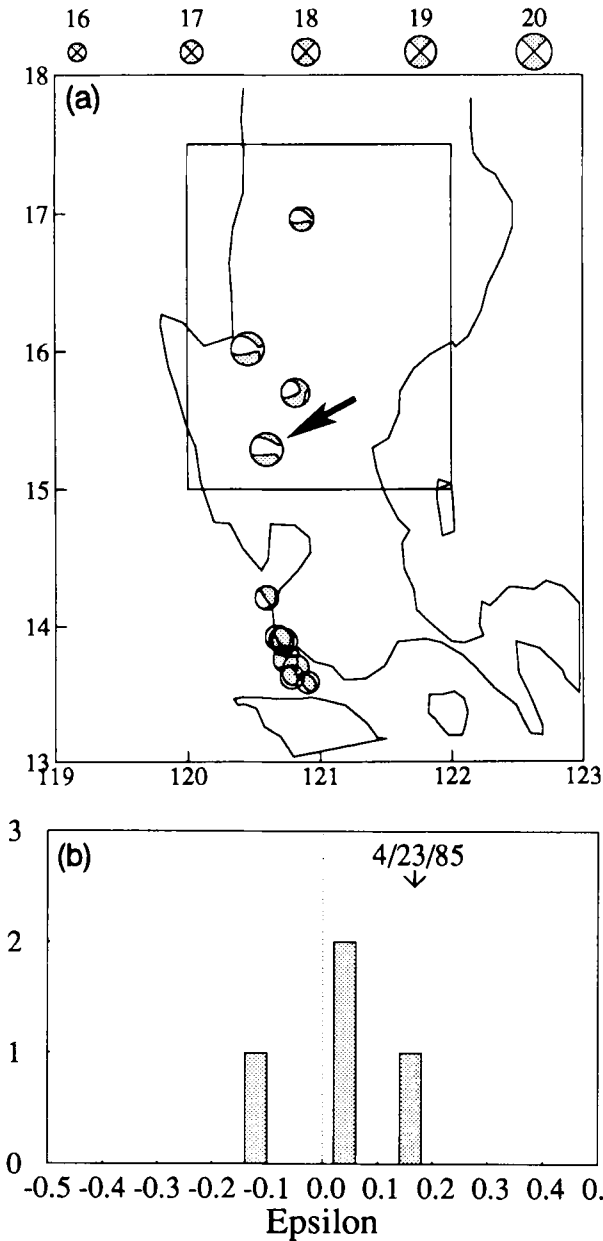


**Figure 2.** The 1985 April 23 Luzon earthquake (depth = 181 km, ISC) and the Harvard CMT solutions in the region (1977–January, 1991; depth  $\geq 100$  km). (a) The map view of the moment tensor solutions. The arrow indicates the Luzon event. (b) The histogram of  $\epsilon$  of the Harvard CMT solutions in the region squared in (a). (c) Directions of the principal axes of the Harvard CMT solutions in the region squared in (a). The directions of the axes are shown on the lower hemisphere projection. Symbols of diamonds, crosses, and triangles correspond to P, N and T axes, respectively. Two dotted lines represent the range of planes which are parallel to the slab and within  $25^\circ$  of the dip angle of the slab on the unit focal sphere. P, N and T in the circle correspond to the principal axes of the Luzon event. P1, N1 and T1 are the principal axes of the first subevent shown in Fig. 1, while P2, N2 and T2 are the axes of the second subevent.

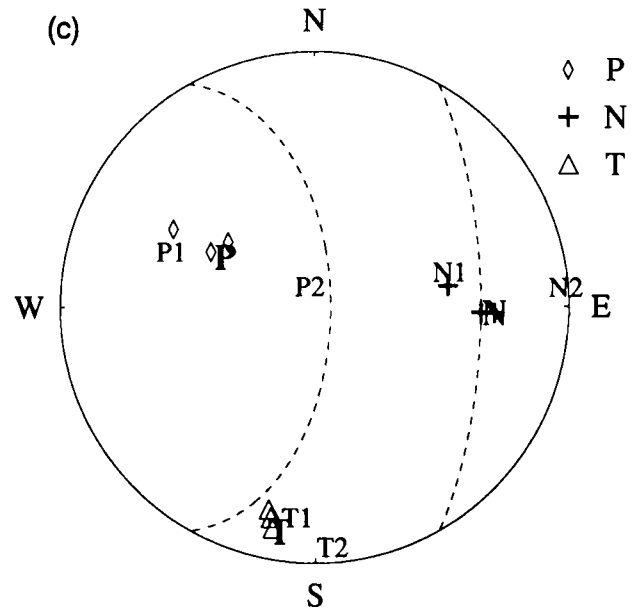


**Figure 2.** (continued)

the slope and intercept of  $\Delta t_{\text{predict}}$  obtained by a least-square means. In the second step, we determine the best  $\delta$  and  $\phi$  by comparing  $V$  in (4) for various pairs of  $\delta$  and  $\phi$  and finding the minimum  $V$ . We search over 144 points at 24 for  $\phi$  and 6 for  $\delta$ . Each cross point in Fig. 4b represents one trial  $(\delta, \phi)$ . The minimum  $V$  is obtained in the direction shown by the star, representing the relative location of the second subevent;  $(\delta, \phi) = (15^\circ, S15^\circ W)$ . The distance between the first and the second subevents is 34 km. Fig. 4b also shows the variation in  $V$ , which is represented by the percentage relative to the minimum  $V$ .  $V$  strongly changes in the azimuthal direction, whereas it is almost constant with a change in dip angle. The location error in  $\delta$  is expected to be large. Fig. 4a shows  $\Delta t_{\text{predict}}$  (a

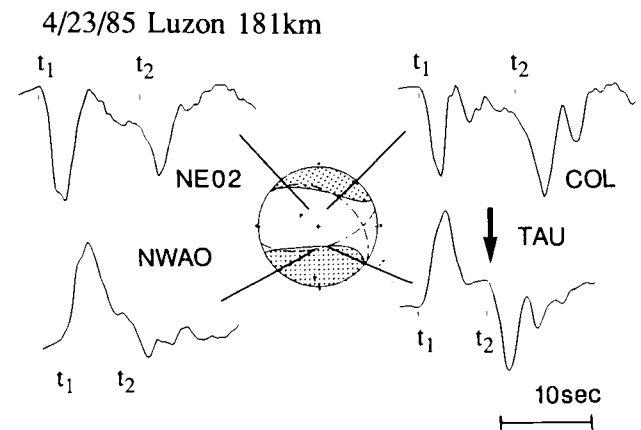


**Figure 3.**  $P$ -wave displacement waveforms from the 1985 April 23 Luzon event. The pass band of the filter is between 0.03 and 1.0 Hz. The focal mechanism solution is estimated from the CMT inversion of long-period body waves. Different polarity between the two subevents is observed at TAU (see an arrow). The times indicated by symbols ' $t_1$ ' and ' $t_2$ ' are read as the phase arrivals from the two subevents, and the differences in time ( $\Delta t = t_2 - t_1$ ) are used in Fig. 4 to estimate the relative location and time of the second subevent.

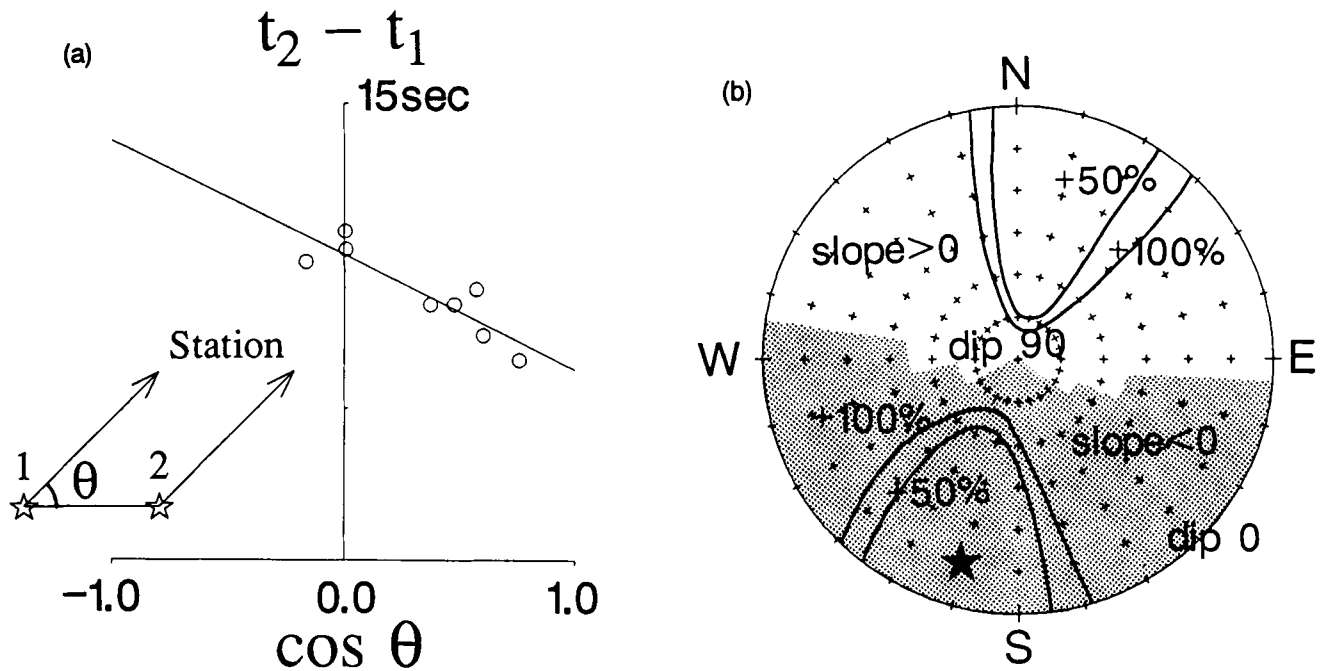


**Figure 4.** Directivity analysis for the second subevent of the 1985 April 23 Luzon event. (a) Directivity of time difference ( $\Delta t = t_2 - t_1$ ) between the arrivals from the two subevents when the second subevent is located at a star position in (b). A circle represents the time difference  $\Delta t_{\text{obs}}^{(i)}$  which is read in a broadband seismogram (see Fig. 3).  $\theta$  is the angle between the station direction along the seismic ray and the direction to the location of the second subevent (see the inserted figure). A solid line is the predicted time difference ( $\Delta t_{\text{predict}}$ ). The slope and y-intercept give the distance and delay time of the second subevent. (b) Variation in total variance estimated from the assumed location of the second subevent. Crosses indicate all the dip and azimuth directions as candidates for the location of the second subevent. For each point, we examined the directivity like (a). Total variance ( $V$ ) is computed from  $\sum_i (\Delta t_{\text{obs}}^{(i)} - \Delta t_{\text{predict}}^{(i)})^2$ , where the superscript 'i' corresponds to the  $i$ th station. Contours represent the increase of the  $V$  relative to the minimum  $V$  obtained at the star position (S15°W, dip = 15°,  $\Delta = 34$  km). A dotted area corresponds to the negative slope of the best-fit line. Note that a negative slope means that a candidate for the location of the second subevent exists in the down-dipping direction, whereas a positive slope means that it is in the upper-dipping direction but the reverse side (azimuth + 180°).

solid line) from the estimated location of the second subevent (the star in Fig. 4b).

Using this relative location and origin time of the second subevent, we obtain a moment tensor solution and a source time function for each subevent. We use seven  $P$ -wave displacement waveforms at GDSN stations and one WWSSN station (KOD), and  $SH$  and  $SV$ -wave displacement waveforms at COL and NE02. The source time function is represented by overlapping triangles whose duration is 1 s. Fig. 5 shows the two moment tensor solutions, and synthetic waveforms compared with the observations. Although the source time functions are shown, the details are not well resolved in this analysis. Table 4 lists the components of the solutions. Both solutions are close to double couple mechanisms; non-double couple components,  $\epsilon$ , of the first and second subevents are 0.05 and 0.03, respectively. The moment tensor of the first subevent includes a significant strike-slip component, whereas the moment tensor of the second subevent is almost pure dip-slip. The polarities of the initial motions of  $P$ -waves shown in Fig. 5 are consistent with the solution of the first subevent. Fig. 6 shows confidence ellipses for the principal axis directions for the two solutions in Fig. 5. Following the method of Riedesel & Jordan (1989), we obtain the ellipses from covariance matrix of moment tensor. The ranges of the 95 per cent confidence level are shown. The ellipses illustrate marginal uncertainties in the

directions of the principal axes induced by variance between observed and synthetic waveforms because the trade-off among the uncertainties in different eigenvectors is not considered (Riedesel & Jordan 1989). For the moment tensors of the two subevents, the discrepancy in dip angle of the  $P$  and  $N$  axes is significant (Fig. 5). In Fig. 6, we cannot, however, observe predominant uncertainties in dip angle of these axes. The principal axes of the first subevent have less uncertainties than those of the second subevent. The  $T$  and  $N$  axes of the second subevent are more unstable in the azimuthal direction than the dip direction, whereas the  $P$  axis is in the vertical direction and stable. It is unlikely that the discrepancy between two moment tensors is caused by the uncertainty induced by noise in the data. In addition, Fig. 5 shows that the two different moment tensors accurately predict the polarity changes between the two subevents at CTAO, SNZO and TAU. Moment tensor solutions of the second subevent obtained in other inversions for various locations of the second subevent show that the moment tensor solution with a significant dip-slip component is stably estimated in the directions  $S$  to  $S30^\circ W$ . A change in subevent focal mechanism is thus significant for this earthquake.

Finally, we compare the sum of the two double couple mechanisms from the broadband analysis with the three solutions from the long-period analysis. The four focal mechanisms are shown in Fig. 1 and Table 3. The solution

### 4/23/85 Luzon (181km)

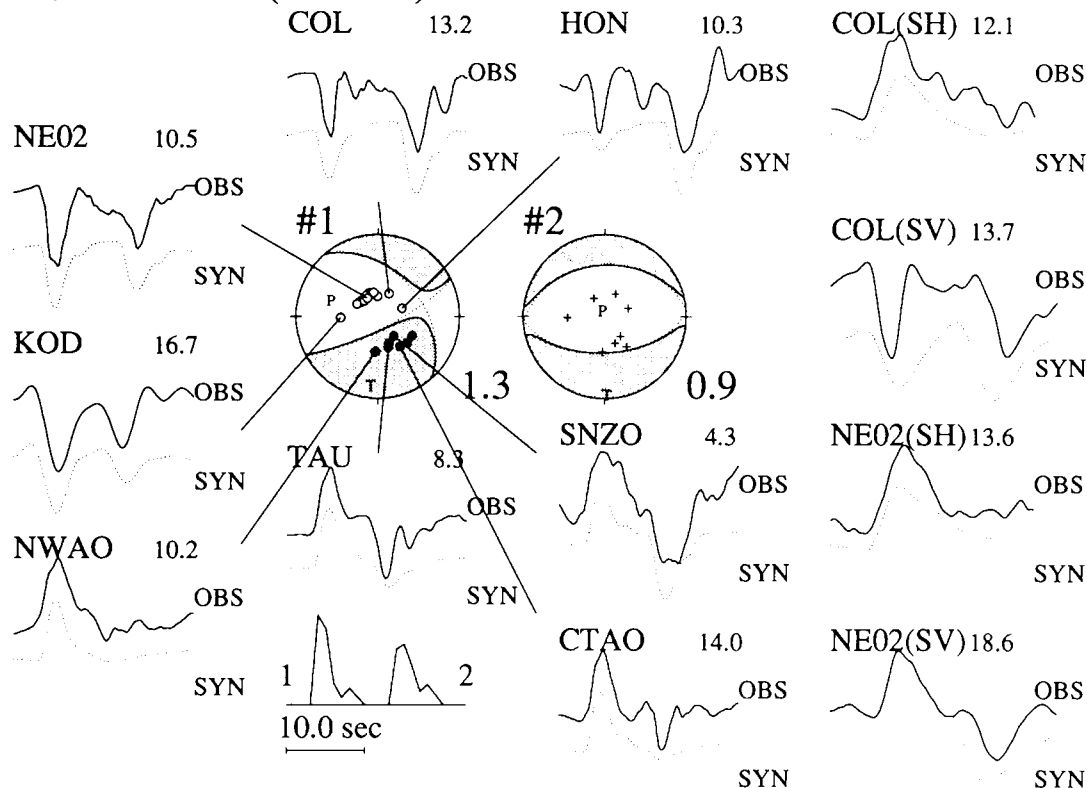


**Figure 5.** Solutions derived from the broadband analysis for the 1985 April 23 Luzon event. Two moment tensor solutions on lower hemisphere projections, source time functions, and displacement seismograms are shown. The waveforms are band-pass filtered between 0.03 and 1.0 Hz. Initial motions in WWSSN and GDSN long-period records are plotted on the solution of the first subevent. Solid and open circles represent compression and dilatation, respectively. Crosses on the solution of the second subevent are the locations of the used stations. Upper and lower waveforms represent the observations and the synthetics computed from two different moment tensors. The number for each station indicates the scaling factor of the waveform amplitude.

under the label 'BB' is the sum of the two double couple sources below it. These double couple mechanisms are estimated from another inversion in the broadband waveform analysis. We use the iterative method of Kikuchi & Kanomori (1991) to satisfy the double couple condition that the determinant of the moment tensor is zero. The double-couple constraint increases the total sum of the squared residuals between the synthetic and observed waveforms by only 3 per cent compared to the previous

**Table 4.** Moment tensor solutions of the two subevents in the broadband waveform analysis for the 1985 April 23 Luzon event (depth = 181 km, ISC).

	#1	#2
$M_0$	1.280	0.868
$M_{xx}$	$1.057 \pm 0.055$	$0.844 \pm 0.079$
$M_{yy}$	$-0.641 \pm 0.056$	$-0.024 \pm 0.075$
$M_{zz}$	$-0.416 \pm 0.027$	$-0.820 \pm 0.046$
$M_{xy}$	$-0.327 \pm 0.072$	$-0.054 \pm 0.108$
$M_{xz}$	$-0.655 \pm 0.024$	$-0.242 \pm 0.038$
$M_{yz}$	$0.507 \pm 0.028$	$-0.005 \pm 0.039$
$\epsilon$	$0.05 \pm 0.03$	$0.03 \pm 0.08$

Unit of  $M_0$  and  $M_{ij}$  is  $\times 10^{19}$  Nm. The error ranges of  $\epsilon$  are estimated in the first-order approximation (equation 6).

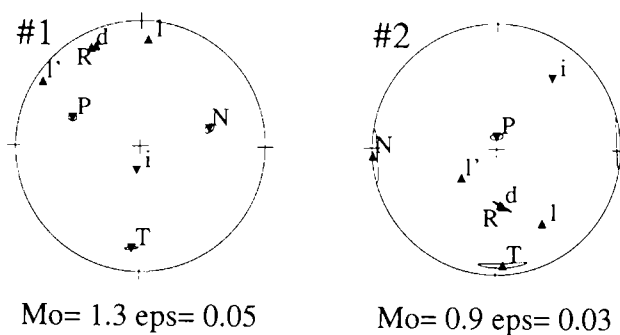


**Figure 6.** The confidence ellipses of the principal axes for the two subevents of the 1985 April 23 Luzon event. P, N and T correspond to the principal axes of the moment tensor. The other symbols follow Riedesel & Jordan (1989). **R** corresponds to the vector which describes a source mechanism:  $\hat{\lambda} = \sum_{i=1}^3 \lambda_i \hat{e}_i$ , where  $\lambda_i$  and  $\hat{e}_i$  are the eigenvalue of the moment tensor ( $\lambda_1 > \lambda_2 > \lambda_3$ ) and the eigenvector, respectively. **d**, **l**, **l'**, and **i** correspond to the vectors for a double couple source, two possible CLVD vectors, and an isotropic source, respectively. The vectors are plotted as downward triangles if they are on the lower hemisphere and as upward triangles if they are projected from the upper hemisphere. The dimension of the ellipse corresponds to the area of the 95 per cent confidence level.

moment tensor inversion. This is because the moment tensor solutions are close to double-couple mechanisms. The non-double couple component ( $\epsilon$ ) in the summed focal mechanism is 0.14. This is close to the one standard deviation range of the non-double couple parameter ( $0.16 < \epsilon < 0.30$ ) obtained from the three solutions at long periods. The summed focal mechanism is thus consistent with the solutions from the long-period waveform analysis. We conclude from the very broadband waveform analysis that the non-double couple component of this earthquake is caused by the combination of the two double couple subevents with different focal mechanisms.

**4 THE 1987 MAY 7 NORTHERN SEA OF JAPAN EARTHQUAKE**

There are significant non-double couple components in the moment tensor solutions obtained from the long-period waveform analysis, which are shown in the left side of Fig. 7 and Table 5. The focal mechanism solutions are similar to each other in the three inversions using different seismic

waves at different frequency bands. The non-double couple component is estimated to be  $-0.22 \pm 0.03$  from the three solutions. It is  $-0.19$  from the Harvard CMT solution (Dziewonski *et al.* 1988). Fig. 8 shows the moment tensor solutions from the CMT single station analysis at some

**Table 5.** Moment tensor solutions in the very broadband waveform analysis of the 1987 May 7 northern Sea of Japan event (depth = 417 km, ISC).

	CMT surface	CMT body	GDSN LP	BB DC	BB M
$M_0$	1.720	1.372	1.773	1.991	1.942
$M_{xx}$	$0.619 \pm 0.031$	$0.459 \pm 0.028$	$0.693 \pm 0.058$	$0.439 \pm 0.069$	$0.592 \pm 0.067$
$M_{yy}$	$-1.418 \pm 0.047$	$-1.029 \pm 0.044$	$-1.465 \pm 0.060$	$-1.426 \pm 0.052$	$-1.438 \pm 0.050$
$M_{zz}$	$0.800 \pm 0.023$	$0.569 \pm 0.023$	$0.772 \pm 0.059$	$0.987 \pm 0.027$	$0.846 \pm 0.026$
$M_{xy}$	$0.847 \pm 0.035$	$0.618 \pm 0.033$	$0.976 \pm 0.062$	$0.919 \pm 0.041$	$0.970 \pm 0.040$
$M_{xz}$	$0.276 \pm 0.014$	$0.209 \pm 0.027$	$0.221 \pm 0.032$	$0.626 \pm 0.015$	$0.386 \pm 0.015$
$M_{yz}$	$0.886 \pm 0.029$	$0.853 \pm 0.038$	$0.855 \pm 0.036$	$1.062 \pm 0.025$	$1.091 \pm 0.024$
$\epsilon$	$-0.22 \pm 0.02$	$-0.20 \pm 0.03$	$-0.25 \pm 0.03$	-0.02	-0.15

Unit of  $M_0$  and  $M_{ij}$  is  $\times 10^{19}$  Nm. The moment tensor solution labelled 'BB(DC)' is the sum of the two double couple sources: 60.7/54.3/159.6 (strike/dip/slip[degree]) ( $M_0 = 0.66$ ) and 53.1/39.0/144.6 ( $M_{ij} = 1.35$ ). The moment tensor solution labelled 'BB(M)' is the sum of the two moment tensors in Table 6. The error ranges of  $\epsilon$  are estimated in the first-order approximation (equation 6).

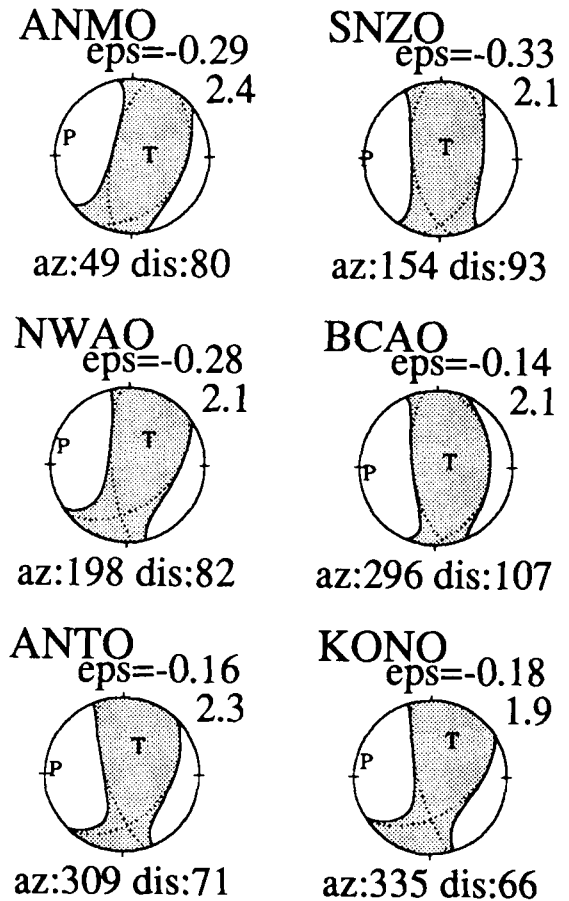


**Figure 8.** Single station CMT solutions of the 1987 May 7 northern Sea of Japan earthquake. The number in the upper-right side of each solution represents the seismic moment [ $\times 10^{19}$  Nm]. The epicentral distance and azimuthal angle of a station are shown in unit of degree.

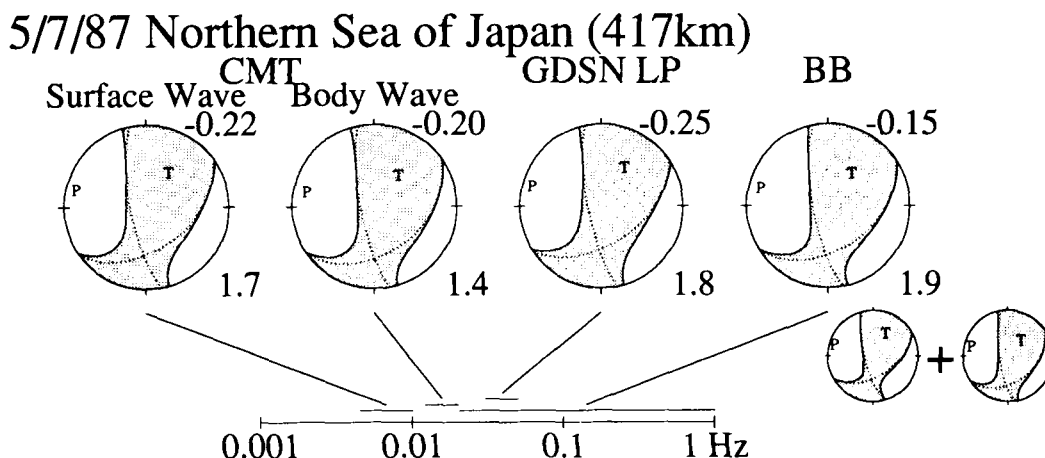


**Figure 7.** Comparison of the moment tensor solutions obtained at four different frequency bands in the very broadband waveform analysis for the 1987 May 7 northern Sea of Japan event (depth = 417 km, ISC). The notation is the same as for Fig. 1.

GDSN stations. Each solution is retrieved from long-period body waves and surface waves recorded at only one station. Although the stations span the azimuthal range from N49°E to N335°E, all the solutions are consistent with each other and show significant deviations from double couple mechanisms. The non-double couple components are estimated to be in the range from  $-0.33$  to  $-0.14$ . The average value of  $\epsilon$  is  $-0.23 \pm 0.08$ . The large non-double couple component of the moment tensor is robust, irrespective of the station used. It is thus unlikely that unmodelled propagation errors can contribute significantly to these non-double couple components. For other deep events in the southwestern Kurile, most non-double couple components are not so significant (Figs 9a and b).

Fig. 10 shows representative *P*-wave broadband displacement waveforms. We observe two major arrivals in

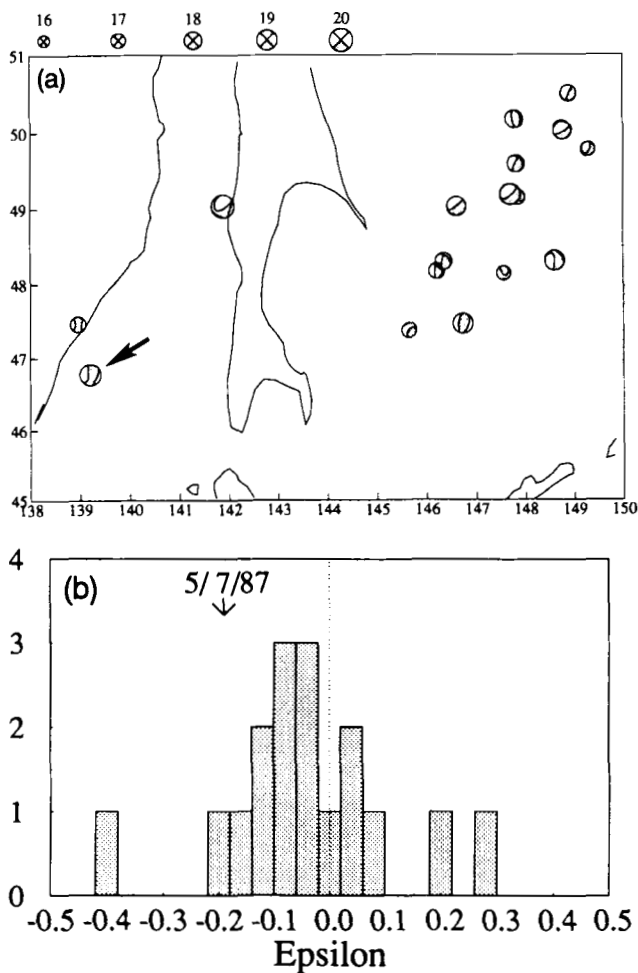


**Figure 9.** The 1987 May 7 northern Sea of Japan earthquake (depth = 417 km, ISC) and the Harvard CMT solutions in the region (1977–January, 1991; depth  $\geq 400$  km). (a) The map view of the moment tensor solutions. The arrow indicates the northern Sea of Japan event. (b) The histogram of  $\epsilon$  of the Harvard CMT solutions shown in (a). (c) Distribution of the principal axes of the Harvard CMT solutions shown in (a). P, N and T in the circle correspond to the principal axes of the northern Sea of Japan event. P1, N1 and T1 are the principal axes of the first subevent shown in Fig. 7, while P2, N2 and T2 are the axes of the second subevent. The other notation is the same as for Fig. 2.

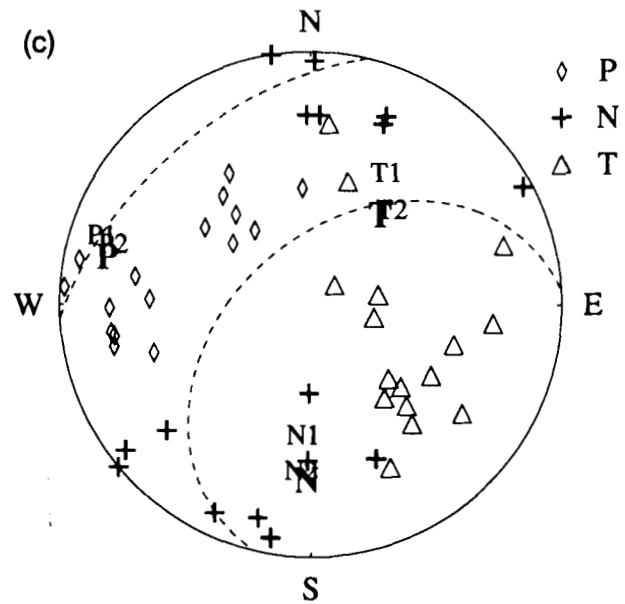


**Figure 9.** (continued)

the waveforms at different epicentral distances. The second phase arrives 4.5 seconds after the initial motions. These are not reflected arrivals such as *PcP* waves, so that rupture process of this earthquake includes at least the two significant subevents. The seismic energy of the second subevent is significant at stations in North America (e.g. COL) which lie far from the nodal planes. Waveforms observed at stations close to the nodal planes change from station to station (e.g. NWA0 and KEV).

To estimate the moment tensors of these two subevents by broadband waveform analysis, we use displacement waveforms at GDSN stations supplemented by WWSSN stations at western azimuths. At the GDSN stations, the second phase arrives  $4.5 \pm 0.4$  s after the initial motion. No significant directivity is found in the time differences

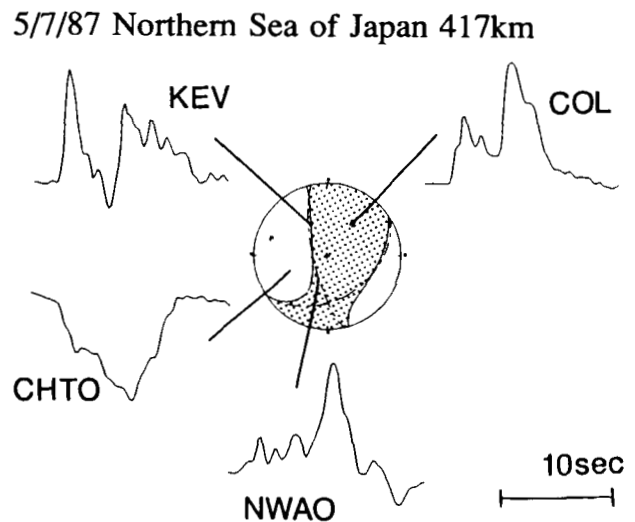


**Figure 10.** *P*-wave displacement waveforms from the 1987 May 7 northern Sea of Japan earthquake. The pass band of the filter is between 0.02 and 1.0 Hz. The focal mechanism solution is estimated from the CMT inversion of long-period body waves.

between the first and second phases. On the other hand, the second phase arrives slightly earlier on the 4 WWSSN long-period seismograms ( $4.0 \pm 0.6$  s). Larger errors are expected in the arrival times read from WWSSN seismograms. It is not clear that this difference in arrival time results from a difference in location between the first and second subevents. The second subevent is, however, assumed to be located 5 km towards N285°E of and 17 km above the location of the first subevent in the following analysis. This prevents any systematic misfit at the WWSSN stations from contaminating our solutions.

Fig. 11 shows the moment tensor solutions obtained for the two subevents, and the observed and synthetic *P*-wave displacement waveforms. Stations in North America are abundant for this event, so we decrease the weight of the data to attain a more homogeneous azimuthal station coverage. We count the number of available stations in every 10° azimuthal range, and use the inverse as a weighting factor in the inversion procedure. The components of the moment tensors are given in Table 6. The half durations of each element of the source time functions are 1 and 1.4 s for the first and second subevents, respectively. The two moment tensor solutions are similar to each other. The total sum of the squared residuals between the synthetic and observed waveforms is almost the same as that from another inversion in which the moment tensors for the two subevents are assumed to be the same. The non-double couple components in the first and second moment tensors

**Table 6.** Moment tensor solutions of the two subevents in the broadband waveform analysis for the 1987 May 7 northern Sea of Japan event (depth = 417 km, ISC).

	#1	#2
$M_0$	0.672	1.282
$M_{xx}$	$0.250 \pm 0.039$	$0.342 \pm 0.045$
$M_{yy}$	$-0.507 \pm 0.031$	$-0.930 \pm 0.040$
$M_{zz}$	$0.257 \pm 0.014$	$0.589 \pm 0.022$
$M_{xy}$	$0.364 \pm 0.021$	$0.606 \pm 0.034$
$M_{xz}$	$0.185 \pm 0.008$	$0.201 \pm 0.012$
$M_{yz}$	$0.308 \pm 0.015$	$0.783 \pm 0.020$
$\epsilon$	$-0.10 \pm 0.02$	$-0.17 \pm 0.03$

Unit of  $M_0$  and  $M_{ij}$  is  $\times 10^{19}$  Nm. The error ranges of  $\epsilon$  are estimated in the first-order approximation (equation 6).

are substantial,  $-0.10$  and  $-0.17$ , respectively. The confidence ellipses for the directions of the principal axes are shown in Fig. 12.

The results of the inversion for double couple mechanisms of the two subevents and the resulting summed moment tensor solution are shown in Table 5. The double couple constraint makes the total sum of the squared residuals between the synthetic and observed waveforms twice that in the previous moment tensor inversion. Since the two subevent mechanisms are similar, we observe little non-double couple component in the summed moment tensor solution. The  $\epsilon$  is  $-0.02$  which is only 9 per cent of the

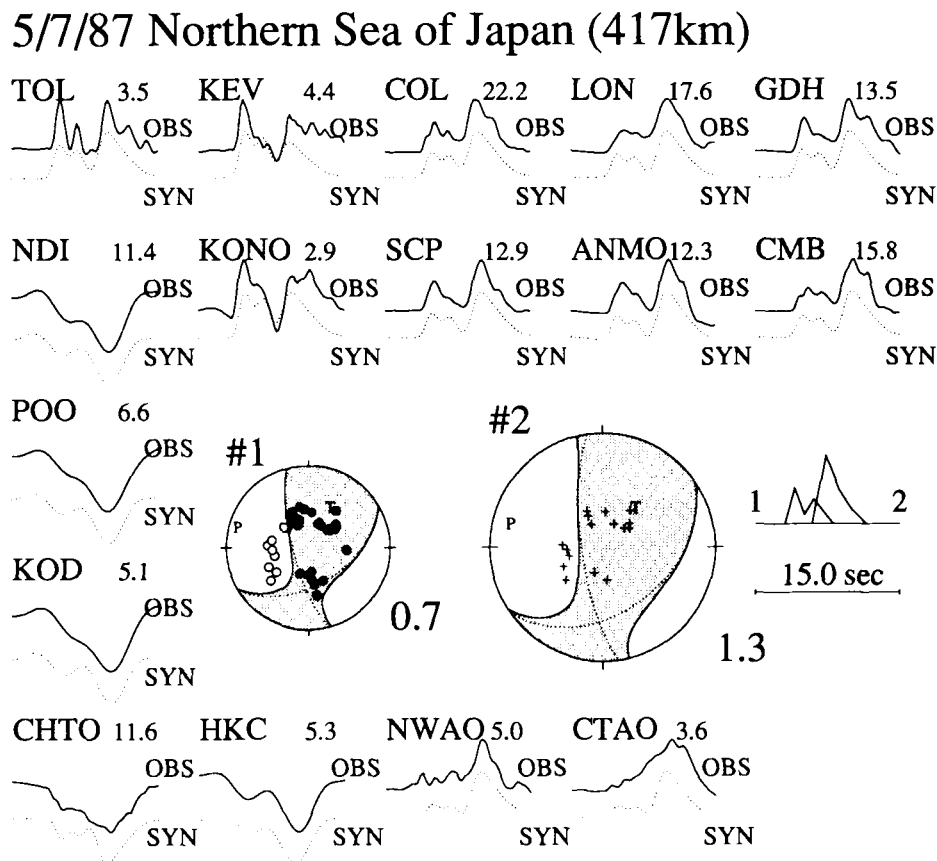


**Figure 11.** Solutions derived from the broadband analysis for the 1987 May 7 northern Sea of Japan event. Two moment tensor solutions on lower hemisphere projections, source time functions, and *P*-wave displacement seismograms are shown. The waveforms are band-pass filtered between 0.02 and 1.0 Hz. The notation is the same as for Fig. 5.

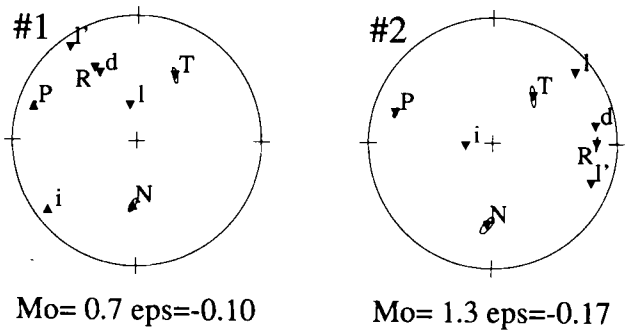


**Figure 12.** The confidence ellipses of the principal axes for the two subevents of the 1987 May 7 northern Sea of Japan earthquake. The dimension of the ellipse corresponds to the area of the 95 per cent confidence level. The notation is the same as for Fig. 6.

non-double couple component estimated at long periods. It is thus difficult to explain the large deviation from a double couple mechanism observed in the long-period waveform analysis only by a combination of two major double couple sources for this event. The moment tensor mechanism under the label 'BB' in Fig. 7 is the sum of the two moment tensor solutions in Fig. 11. The non-double couple component of the summed moment tensor is  $-0.15$ . It is more consistent with the solutions in the long-period analysis. Non-double couple components of the two subevents seem to be inescapable, but our inversion cannot resolve whether each subevent is itself a composite of multiple double couple sources.

### 5 THE 1984 JANUARY 1 SOUTH OF HONSHU EARTHQUAKE

Fig. 13 shows the results from the very broadband analysis of the 1984 January 1 south of Honshu earthquake from our earlier work (Kuge & Kawakatsu 1990). We found consistent focal mechanisms obtained at long periods, all of which show large deviations from a double couple

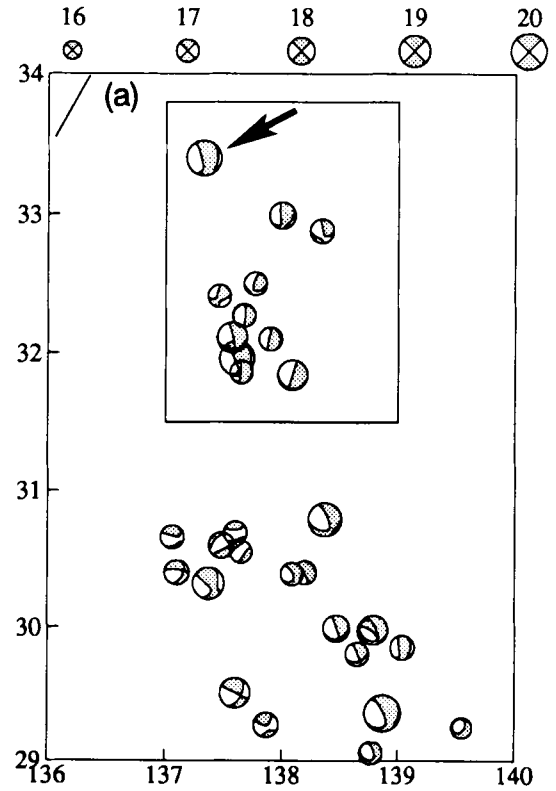


**Figure 14.** The 1984 January 1 south of Honshu earthquake (depth = 386 km, ISC) and the Harvard CMT solutions in the region (1977–January, 1991; depth  $\geq 300$  km). (a) The map view of the moment tensor solutions. The arrow indicates the south of Honshu event. (b) The histogram of  $\epsilon$  of the Harvard CMT solutions in the region squared in (a). (c) Directions of the principal axes of the Harvard CMT solutions in the region squared in (a). P, N and T in the circle correspond to the principal axes of the south of Honshu event. P1, N1 and T1 are the principal axes of the first subevent shown in Fig. 13, while P2, N2 and T2 are the axes of the second subevent. The other notation is the same as for Fig. 2.

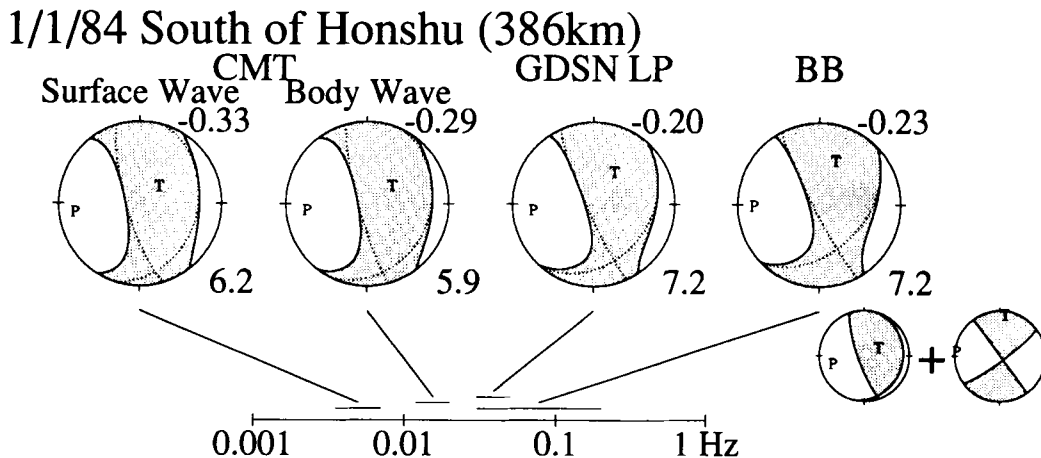


**Figure 13.** Comparison of the moment tensor solutions obtained at four different frequency bands in the very broadband waveform analysis for the 1984 January 1 south of Honshu event (depth = 386 km, ISC) (Kuge & Kawakatsu 1990). The notation is the same as for Fig. 1.

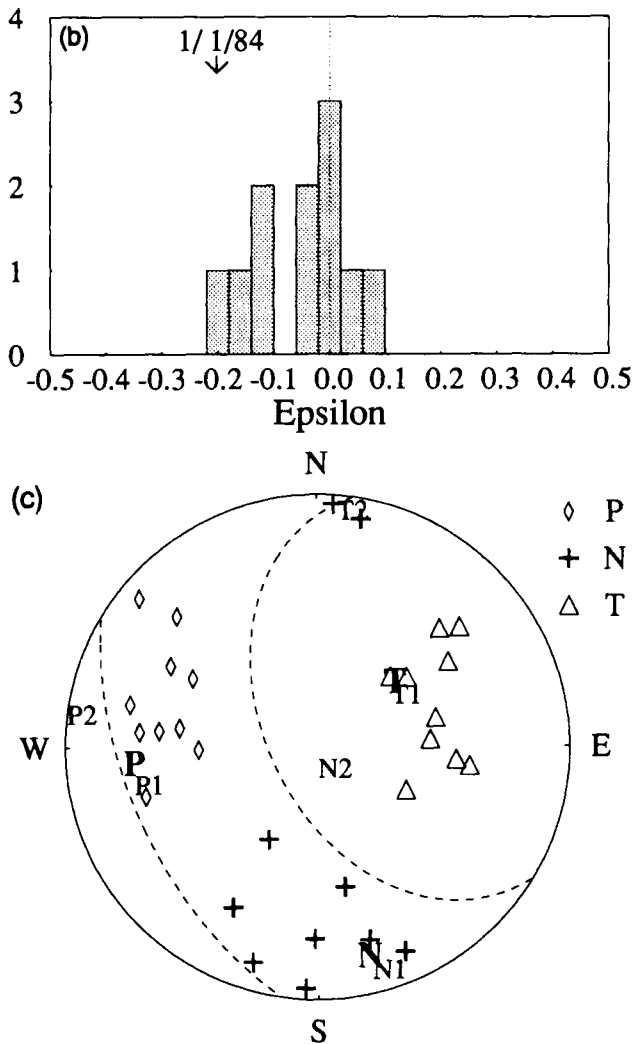


Figure 14. (continued)

mechanism. The non-double couple component from the three solutions is  $-0.27 \pm 0.07$ . Single station CMT analysis (Ekström *et al.* 1986) showed that the large non-double couple component is not an artifact introduced by unmodelled propagation errors. Other deep events, south of Honshu, do not have significant  $\epsilon$  (Figs 14a and b). Kuge & Kawakatsu (1990) pointed out two major phases in the broadband *P*-wave waveforms with relative amplitudes that vary from station to station. The double couple mechanisms in the right end of Fig. 13 were retrieved by modelling the phases. The sum of the double couple sources under the label 'BB' is consistent with the moment tensor solutions from the long-period waveform analysis. The non-double couple component of the summed focal mechanism is  $-0.23$ . The combination of different double couple sources causes a large deviation from a double couple source for this event.

## 6 NON-DOUBLE COUPLE COMPONENTS AND STRAIN STATES WITHIN SUBDUCTING SLABS

Following the definition of a non-double couple component,  $\epsilon$ , the sign of  $\epsilon$  represents which principal strain is more

predominant, compressional or tensional strain. A positive non-double couple component ( $\epsilon > 0$ ) means that the maximum absolute eigenvalue is for the tensional principal axis (T-axis), i.e. predominantly tensional strain. Negative  $\epsilon$  means that the maximum absolute eigenvalue is for the compressional principal axis (P-axis), i.e. predominantly compressional strain. It has been pointed out that the statistical nature of non-double couple components of intermediate-depth and deep events tends to reflect the strain states within subducting slabs both in global and regional scales (Giardini 1983, 1984; Kuge & Kawakatsu 1992). This relation may also be true for the three events in this study.

For south of Honshu, Japan, Fig. 14c presents the directions of the principal axes of the events which are enclosed by the small square in Fig. 14a. The axes are shown on a lower-hemisphere projection. The dotted lines represent a range of planes which are parallel to the slab and within  $25^\circ$  of the dip angle of the slab on the unit focal sphere. Fujita & Kanamori (1981) defined 'in-plate' events as those with principal axes appearing in a similar range on the focal sphere to that between these dotted lines. The P-axes of the deep events are inclined in the direction of the slab dip and appear between two dotted lines. Compressional strain is predominant within the slab. The non-double couple components of the deep events in this region tend to be negative (Fig. 14b;  $\bar{\epsilon} = -0.06 \pm 0.09$ ), consistent with the predominantly compressional strain. The P, N and T in the circle correspond to the principal axes of the south of Honshu event. The compressional axis appears within the dipping slab and the non-double couple component is negative.

For Luzon, Fig. 2c shows the directions of the principal axes of the events which are enclosed by the inset square in Fig. 2a. The T-axes of the intermediate-depth events, including the Luzon event, are aligned in the NS direction and lie in the plane of the subducting slab. On the other hand, the P-axes are inclined vertical to the subducting slab. The regional strain within the slab is predominantly in tension. The non-double couple component of the Luzon event is positive, which is consistent with the regional strain state.

For the northern Sea of Japan and southwestern Kurile arc, Fig. 9a shows Harvard CMT solutions (depth  $\geq 400$  km). There is only one Harvard CMT solution near the northern Sea of Japan event. Even in the bulletins from the International Seismological Center (ISC), seismic activity in this region is low. On the other hand, many deep events occur in the southwestern part of the Kurile slab. Fig. 9c shows the directions of the principal axes of the deep events. The P-axes are inclined from west to northwest, which is consistent with the direction of the downdipping slab shown by dotted lines. Compressional strain is predominant within the southwestern Kurile slab. The moment tensor solution of the northern Sea of Japan event is similar to some deep events in the southwestern part of Kurile (Fig. 9a). The northern Sea of Japan event may have occurred in a similar slab environment to the other deep events, with the predominantly compressional strain state. The non-double couple component of the northern Sea of Japan event is negative.

Change in focal mechanism between subevents can cause

**Table 7.** Difference in direction between the principal axes of two subevents.

	1/1/84 (386 km)	4/23/85 (181 km)	5/7/87 (417 km)
$\Delta$ (T axis)	64.3	14.9	12.1
$\Delta$ (N axis)	73.6	44.2	12.5
$\Delta$ (P axis)	23.0	46.7	5.6
$\epsilon$	—	+	—
strain	compression	tension	compression

Difference in direction between the principal axes of two subevents in each earthquake is presented in angle [degree], which is computed using the double couple focal mechanisms in Table 3 and Table 2 of Kuge & Kawakatsu (1990), and the moment tensor solutions in Table 6. Also shown is a predominant in-plate strain whose related principal axes of the other events in each region tend to appear within the slab (see Figs 2, 9 and 14).

these non-double couple components which reflect the predominant strains within the subducting slabs. The focal mechanisms of two subevents were determined for the three events. We compare the three pairs of principal directions (P, N and T axes) for each event. Table 7 shows the results. For the south of Honshu event, the change in the compressional direction (P-axis) between the two subevents is the smallest of the three axes. The P-axes are within the slab (Fig. 14c). The differences in T-axis and N-axis directions are about three times larger than the difference in P-axis. For the Luzon event, the difference of the tensional principal axis (T-axis) between the two subevents is the smallest. The T-axes are within the slab (Fig. 2c). The

differences in P-axis and N-axis are about three times larger than the difference in T-axis. In the case of the northern Sea of Japan event, the P-axis changes least of the three axes. For any of the three principal axes, however, the changes in direction are small (Fig. 9c) because the mechanisms of the two subevents are similar to each other and the change does not contribute to a significant non-double couple component. Fig. 15 schematically illustrates our suggestion. The principal axes of the subevents, which are likely to be related to the predominant strain within the slab, are close to each other, whereas the other two principal axes rotate around the predominant strain direction, perhaps due to pre-existing zones of weakness. The rotation of the two axes can produce the non-double couple components which are observed at long periods, and show a relationship between non-double couple components and strain state within the slab.

## 7 DISCUSSION

### 7.1 Focal mechanisms of subevents

We now discuss further the difference in focal mechanism between the subevents. The seismic moments of the two subevents for the south of Honshu event are almost the same, whereas the focal mechanisms are different. The focal mechanism of the first subevent is similar to those in the region. On the other hand, the focal mechanism of the second subevent is nearly pure strike-slip. We found a few focal mechanisms similar to the second subevent in the Harvard CMT solutions, but they seem to be rather unusual. The two subevents of the Luzon event also have

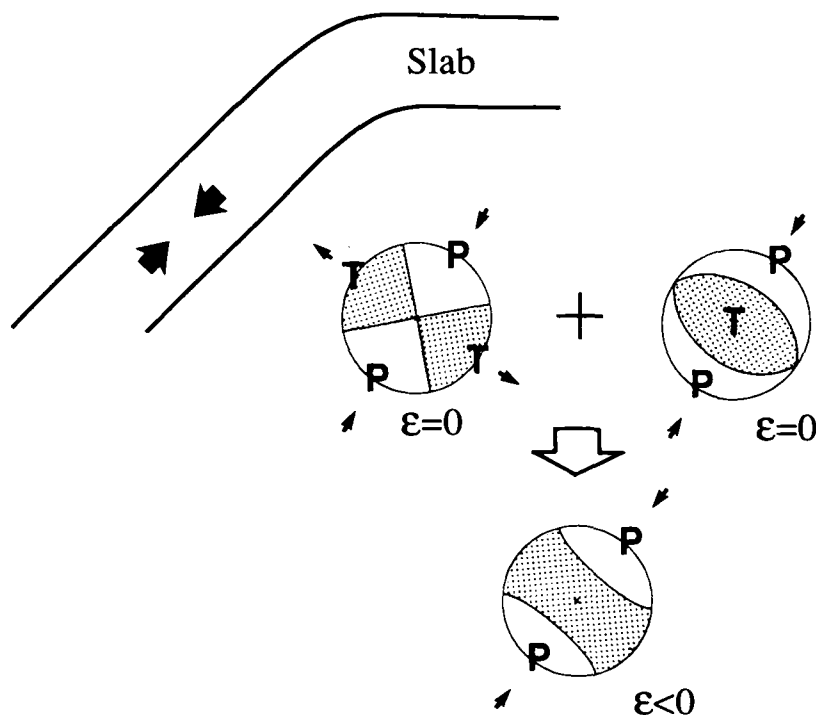


**Figure 15.** Schematic explanation of non-double couple earthquakes in the regime of predominantly compressional strain state within subducting slabs. The principal axis related to the predominant strain is quite stable, whereas the other two principal axes rotate around the direction of the predominant strain. In the case of predominantly tensional strain state, all the arrows point to the reverse directions, and the P and T axes are exchanged with each other. A positive non-double couple component thus results.

similar seismic moments. Just north of this event an intermediate-depth event occurred whose focal mechanism is the same as for the first subevent. On the other hand, we do not find any Harvard CMT solutions with focal mechanisms similar to that of the second subevent. The two subevents of the northern Sea of Japan event have almost the same focal mechanism. Similarly oriented events are observed at the southwestern end of the Kurile slab. It appears that the focal mechanism of the first subevents tend to be consistent with focal mechanisms occurring within the slab, whereas the focal mechanisms of the second subevents, which are probably induced or nucleated by the first subevent, may be rather exceptional.

For shallow events, aftershocks with different focal mechanisms are often induced by a main shock, e.g. the 1990 Luzon event (Yoshida & Abe 1992). For the 1976 July 27 Tangshan and 1988 December 7 Spitak events, it has been especially proposed that several subevents with different focal mechanisms occurred during the rupture process; a strike-slip main pulse and a thrust subevent in the Tangshan event (Kikuchi & Kanomori 1986; Nábělek, Chen & Ye 1987) and a main event with a significant strike-slip component and a reverse-faulting subevent in the Spitak event (Kikuchi *et al.* 1992). These sequences are qualitatively similar to that of the Luzon event, and even the south of Honshu event after rotating the principal axes. Kawakatsu (1991b) suggested that combinations of different focal mechanisms, for example, normal and strike-slip faults, is one of the most likely origins of non-double couple components for Harvard CMT solutions in ridge-transform fault zones. Although the basic physical mechanisms may be different, deep events may induce different focal mechanisms for subevents in the same way as for shallow events.

On the other hand, it seems difficult to argue that the second subevents resulted from stress perturbations by the first subevents, given that the sizes of the subevents are similar for all three deep events. The second subevent might be controlled by some geometrical feature, such as a previous fault which was produced before or during subduction of the slab.

## 7.2 Non-double couple component of the northern Sea of Japan earthquake

Non-double couple components are observed in the moment tensor solutions of each subevent in the northern Sea of Japan earthquake (Fig. 11). Although a non-double couple component ( $\epsilon$ ) is not a linear parameter of the components of moment tensor and the error estimate of  $\epsilon$  is rather complicated (e.g. Vasco 1990) when the covariance matrix of the moment tensor components is not diagonal, we show the significance of the non-double couple components for the northern Sea of Japan event, compared with the Luzon event, by first-order perturbation theory.

Riedesel & Jordan (1989) developed a method for the graphical display of moment tensor on which the statistical significance of non-double couple components can be tested by first-order perturbation theory. Figs 6 and 12 are obtained in their method. The symbol  $\mathbf{R}$  corresponds to the vector which describes the source mechanism,

$$\hat{\lambda} = \sum_{i=1}^3 \lambda_i \hat{e}_i, \quad (5)$$

where  $\lambda_i$  and  $\hat{e}_i$  are the eigenvalue of moment tensor ( $\lambda_1 > \lambda_2 > \lambda_3$ ) and the eigenvector, respectively. The symbols  $\mathbf{d}$ ,  $\mathbf{l}$ ,  $\mathbf{l}'$ , and  $\mathbf{i}$  correspond to the vectors for a double couple source, two possible CLVD vectors, and an isotropic source, respectively. In a case that a source mechanism is a purely double couple,  $\hat{\lambda}$  should be equal to  $\mathbf{d}$ . In a case that a source is CLVD,  $\hat{\lambda}$  should be equal to  $\mathbf{l}$  or  $\mathbf{l}'$ . The confidence ellipse of  $\hat{\lambda}$  is computed from covariance matrix of moment tensor (Riedesel & Jordan 1989). For the Luzon event (Fig. 6), the ellipses ( $2\sigma$ ) of  $\hat{\lambda}$  for the two subevents are very close to the double couple vectors  $\mathbf{d}$ . On the other hand, Fig. 12 for the northern Sea of Japan event shows that the ellipses of  $\hat{\lambda}$  for the two subevents tend to be away from the double couple vectors  $\mathbf{d}$ , especially for the second subevent.

We also estimate the first-order ranges of  $\epsilon$  as follows,

$$\epsilon \pm \Delta\epsilon \approx \frac{\lambda_2 \pm \delta\lambda_2}{\lambda_i \pm \delta\lambda_i} \approx \frac{\lambda_2}{\lambda_i} \left( 1 \pm \frac{\delta\lambda_2}{\lambda_2} \pm \frac{\delta\lambda_i}{\lambda_i} \right) \quad (6)$$

$$(i = 1 \text{ if } |\lambda_1| > |\lambda_3|; i = 3 \text{ if } |\lambda_1| < |\lambda_3|)$$

where  $\lambda_i$  is the eigenvalue of moment tensor ( $\lambda_1 > \lambda_2 > \lambda_3$ ) and  $\delta\lambda_i$  is the standard deviation. The non-double couple components ( $\epsilon$ ) of the first and second subevents in the Luzon event are estimated to be  $0.05 \pm 0.03$  and  $0.03 \pm 0.08$ , respectively. On the other hand, for the northern Sea of Japan event,  $\epsilon$  are  $-0.10 \pm 0.02$  for the first subevent, and  $-0.17 \pm 0.03$  for the second subevent. The non-double couple components are significant.

Since we observe the consistent non-double couple components in our inversions of different seismic waves at different frequency bands, the non-double couple components for this event should be caused by the source itself or the unmodelled near-source structure which have common effects on the radiations of different seismic waves.

One possibility to explain these non-double couple moment tensors of the two subevents for the northern Sea of Japan event is that they are individually caused by a combination of different double couple sources in the same way as observed for the south of Honshu and the Luzon events. We actually observe several additional phases in the broadband displacement waveforms contributing to the two major ones which we modelled (Fig. 11). Changes in focal mechanism might occur at short or zero time delays that we cannot resolve, perhaps producing the large non-double couple components in the moment tensors of the two subevents.

Kawasaki & Tanimoto (1981) pointed out that an anisotropic elastic property of medium around a double couple source can apparently distort the nodal planes in the seismic radiation. For example, when a displacement occurs on a plane in an anisotropic medium whose elastic constants follow the single crystal of olivine in Kumazawa & Anderson (1969), we observe at most 0.2 for  $|\epsilon|$ , although this is accompanied by an isotropic component of  $\sim 20$  per cent. The possibility of anisotropy within a subducting slab was pointed out by Anderson (1987). Alternatively, for long-period seismic waves, the effect of the existence of high velocity slab itself may be similar to that of an anisotropic medium near the source; the slab causes the velocity of seismic waves to be relatively fast in the direction within the slab, whereas it is relatively slow in the direction

perpendicular to the slab. For this anisotropic effect, negative  $\varepsilon$  can result from double couple sources with the principal compressional axes that lie within the slab (Kuge & Kawakatsu 1992).

Knopoff & Randall (1970) predicted the radiation patterns with non-double couple components in cases that elastic properties vary in the source volumes, for example, because of phase transition. When the elastic property is isotropic both before and after phase transition, change in  $\mu$  in the axial strain field can cause non-double couple components, where isotropic elastic constant is  $C_{ijkl} = \lambda\delta_{ij}\delta_{kl} + \mu(\delta_{ik}\delta_{jl} + \delta_{il}\delta_{jk})$ . Especially, decrease in  $\mu$  can contribute to positive  $\varepsilon$  for tensional strain in the source region and negative  $\varepsilon$  for compressional strain, which is consistent with Giardini (1983, 1984) and Kuge & Kawakatsu (1992). Note that change in  $\mu$  in the shear strain field cannot cause any non-double couple components in the radiation. On the other hand, when the elastic property in a source volume is anisotropic before or after phase transition or both, non-double couple components can be caused by change of the elastic property not only in the axial strain field but also in the shear strain field, and the situation should be very complicated. One possible physical mechanism for deep earthquakes is that the phase transition from  $\alpha$ -olivine to  $\beta$ -spinel nucleates a shear dislocation (Green & Burnley 1989). When the crystal axes of spinel within a dislocation region are regularly aligned under non-hydrostatic pressure, we might expect even significant non-double couple components; for example,  $\varepsilon$  is estimated to be 0.24 when the b and c crystal axes of  $\beta$ -Mg<sub>2</sub>SiO<sub>4</sub> (Sawamoto *et al.* 1984) are aligned with the principal compressional and tensional strain directions in the source volume, respectively.

The non-double couple components of the subevents of the northern Sea of Japan event are in a range between  $-0.08$  and  $-0.20$ . The non-double couple component for the entire event is  $-0.23 \pm 0.08$  in the long-period analysis. On the other hand,  $\varepsilon$  of deep events in the southwestern Kurile is  $-0.01 \pm 0.13$  (Fig. 9). For deep events (depth  $\geq 300$  km) in the world,  $\varepsilon$  is  $-0.04 \pm 0.14$  (Kuge & Kawakatsu 1992). The non-double couple component of the northern Sea of Japan event, even of each subevent, tends to be more significant than those of other deep events in the southwestern Kurile and in other regions. Therefore, even if a near-source anisotropic effect or an intrinsic non-double couple source caused the significant non-double couple component of the northern Sea of Japan event, the cause should not contribute significantly to non-double couple components for other deep events and it should be significant only for this event. Although the properties within slabs and the physical mechanisms of deep earthquakes are not resolved well, it may be difficult to consider these situations. Combinations of different double couple sources appear to explain the non-double couple component for the northern Sea of Japan event most simply.

## 8 CONCLUSIONS

Based on clear evidence from two earthquakes, the 1985 April 23 Luzon and 1984 January 1 south of Honshu events, we suggest that non-double couple moment tensors of intermediate-depth and deep earthquakes result from the

combination of different double couple subevents which are oriented by predominant strain regime within the slab. We obtain consistent non-double couple focal mechanisms using different seismic waves in various frequency bands. Modelling the broadband waveforms, we found two subevents with different double couple mechanisms for each earthquake. Superposition of the different double couple mechanisms produces the non-double couple moment tensors obtained at long periods. Of the principal axes of the subevents, those which are oriented with the predominant strain state within the slab are stable between the subevents, whereas the other two principal axes rotate around the direction of the predominant strain. This interpretation may explain global and regional trends of non-double couple components in relation to the slab geometry. For another deep non-double couple event, the 1987 May 7 northern Sea of Japan earthquake, very stable and consistent non-double couple focal mechanisms are found using different seismic waves at long periods, whereas each subevent which we model in this study has a similar non-double couple mechanism. Analysing each subevent as a double couple does not explain the overall non-double couple radiation. An unresolved change of double couple mechanisms in each event may contribute as the non-double couple component of the subevent, and appears to explain the overall deviation from a double couple source most simply.

## ACKNOWLEDGMENTS

We thank S. Watada for sending the GDSN data of the 1987 May 7 northern Sea of Japan event. We thank T. Lay, K. Oike and J. Zhang for reviewing the manuscript. Completion of this work at UCSC was partially supported by NSF Grant EAR-8451715 and the W. M. Keck Foundation, while K. Kuge received support from the Japan Society for the Promotion of Science. Contribution No. 150 of the Institute of Tectonics and C. F. Richter Seismological Laboratory at the University of California, Santa Cruz.

## REFERENCES

- Anderson, D. L., 1987. Thermally induced phase changes, lateral heterogeneity of the mantle, continental roots, and deep slab anomalies, *J. geophys. Res.*, **92**, 13968–13980.
- Billington, S. & Isacks, B. L., 1975. Identification of fault planes associated with deep earthquakes, *Geophys. Res. Lett.*, **2**, 63–66.
- Burnley, P. C., Green, H. W., II. & Prior, D. J., 1991. Faulting associated with the olivine to spinel transformation in Mg<sub>2</sub>GeO<sub>4</sub> and its implications for deep-focus earthquakes, *J. geophys. Res.*, **96**, 425–553.
- Choy, G. L. & Boatwright, J., 1981. The rupture characteristics of two deep earthquakes inferred from broadband GDSN data, *Bull. seism. Soc. Am.*, **71**, 691–711.
- Doornbos, D. J., 1985. Source solutions and station residuals from long-period waveform inversion of deep events, *J. geophys. Res.*, **90**, 5466–5478.
- Dziewonski, A. M. & Anderson, D. L., 1981. Preliminary reference Earth model, *Phys. Earth planet. Int.*, **25**, 297–356.
- Dziewonski, A. M., Chou, T. A. & Woodhouse, J. H., 1981. Determination of earthquake source parameters from waveform data for studies of global and regional seismicity, *J. geophys. Res.*, **86**, 2825–2852.
- Dziewonski, A. M., Ekström, G., Woodhouse, J. H. & Zwart, G.,

1988. Centroid-moment tensor solutions for April–June 1987, *Phys. Earth planet. Int.*, **50**, 215–225.
- Dziewonski, A. M., Frazen, J. E. & Woodhouse, J. H., 1986. Centroid-moment tensor solutions for April–June 1985, *Phys. Earth planet. Int.*, **41**, 215–224.
- Dziewonski, A. M., & Woodhouse, J. H., 1983a. Studies of the seismic source using normal-mode theory, in *Earthquakes: observation, theory and interpretation*, pp. 45–137, ed Kanamori, H. & Bosch, E., North-Holland, Amsterdam.
- Dziewonski, A. M. & Woodhouse, J. H., 1983b. An experiment in systematic study of global seismicity: centroid-moment tensor solutions for 201 moderate and large earthquakes in 1981, *J. geophys. Res.*, **88**, 3247–3271.
- Ekström, G., & Dziewonski, A. M., 1985. Centroid-moment tensor solutions for 35 earthquakes in western north America (1977–1983), *Bull. seism. Soc. Amer.*, **75**, 23–39.
- Ekström, G., Dziewonski, A. M. & Steim, J. M., 1986. Single station CMT; application to the Michoacan, Mexico, earthquake of September 19, 1985, *Geophys. Res. Lett.*, **13**, 173–176.
- Frohlich, C., 1989. The nature of deep-focus earthquakes, *Ann. Rev. Earth planet. Sci.*, **17**, 227–254.
- Frohlich, C., Riedesel, M. A. & Apperson, K. D., 1989. Note concerning possible mechanisms for non-double couple earthquake sources, *Geophys. Res. Lett.*, **16**, 523–526.
- Fujita, K. & Kanamori, H., 1981. Double seismic zones and stresses of intermediate depth earthquakes, *Geophys. J. R. astr. Soc.*, **66**, 131–156.
- Fukao, Y., 1972. Source process of a large deep-focus earthquake and its tectonic implications—the western Brazil earthquake of 1963, *Phys. Earth planet. Interiors*, **5**, 61–76.
- Giardini, D., 1983. Regional deviation of earthquake source mechanisms from the ‘double-couple’ model in: *Earthquakes: theory and interpretation*, pp. 345–353, ed. Kanamori, H. & Bosch, E., North-Holland, Amsterdam.
- Giardini, D., 1984. Systematic analysis of deep seismicity: 200 centroid-moment tensor solutions for earthquakes between 1977 and 1980, *Geophys. J. R. astr. Soc.*, **77**, 883–914.
- Giardini, D. & Woodhouse, J. H., 1984. Deep seismicity and modes of deformation in Tonga subduction zone, *Nature*, **307**, 505–509.
- Gilbert, F., & Dziewonski, A. M., 1975. An application of normal mode theory to the retrieval of structural parameters and source mechanisms from seismic spectra, *Phil. Trans. R. Soc. London A*, **278**, 187–269.
- Green, H. W., II & Burnley, P. C., 1989. A new self-organizing mechanism for deep-focus earthquakes, *Nature*, **341**, 733–737.
- Green, H. W., II, Young, T. E., Walker, D. & Scholz, C. H., 1990. Anticrack-associated faulting at very high pressure in natural olivine, *Nature*, **348**, 720–722.
- Griggs, D. T. & Baker, D. W., 1969. The origin of deep-focus earthquakes, in *Properties of Matter Under the Usual Conditions*, pp. 23–42, eds, Mark, H. & Fernback, S. Wiley Interscience, New York.
- Griggs, D. T. & Handin, J. 1960. Observations on fracture and a hypothesis of earthquakes, in: *Rock Deformation*, D. T. Griggs and J. Handin, eds., Geological Society of America Memoir, **79**, 347–373.
- Harvey, D. & Choy, G. L., 1982. Broadband deconvolution of GDSN data, *Geophys. J. R. astr. Soc.*, **69**, 659–668.
- Hobbs, B. E. & Ord, A., 1988. Plastic instability: implications for the origin of intermediate and deep focus earthquakes, *J. geophys. Res.*, **93**, 10521–10540.
- Isacks, B. & Molnar, P., 1971. Distribution of stresses in the descending lithosphere from a global survey of focal-mechanism solutions of mantle earthquakes, *Rev. Geophys. Space Phys.*, **9**, 103–174.
- Kawakatsu, H., 1989. Centroid single force inversion of seismic waves generated by landslides, *J. geophys. Res.*, **94**, 12363–12374.
- Kawakatsu, H., 1991a. Insignificant isotropic component in the moment tensor of deep earthquakes, *Nature*, **351**, 50–53.
- Kawakatsu, H., 1991b. Enigma of earthquakes at ridge-transform-fault plate boundaries—distribution of non-double couple parameter of Harvard CMT solutions, *Geophys. Res. Lett.*, **18**, 1103–1106.
- Kawasaki, I. & Tanimoto, T., 1981. Radiation patterns of body waves due to the seismic dislocation occurring in an anisotropic source medium, *Bull. seism. Soc. Am.*, **71**, 37–50.
- Kikuchi, M. & Kanamori, H., 1986. Inversion of complex body waves—II, *Phys. Earth planet. Int.*, **43**, 205–222.
- Kikuchi, M. & Kanamori, H., 1991. Inversion of complex body waves—III, *Bull. seism. Soc. Am.*, **81**, 2335–2350.
- Kikuchi, M., Kanamori, H. & Satake, K., 1992. Source complexity of the 1988 Armenian earthquake—evidence for a slow after-slip event, *J. geophys. Res.*, submitted.
- Kirby, S. H., 1987. Localized polymorphic phase transformations in high-pressure faults and applications to the physical mechanism of deep earthquakes. *J. geophys. Res.*, **92**, 13789–13800.
- Kirby, S. H., Durham, W. B. & Stern, L. A., 1991. Mantle phase changes and deep-earthquake faulting in subducting lithosphere, *Science*, **252**, 216–225.
- Knopoff, L. & Randall, M. J., 1970. The compensated linear-vector dipole: a possible mechanism for deep earthquakes, *J. geophys. Res.*, **75**, 4957–4963.
- Kuge, K. & Kawakatsu, H., 1990. Analysis of a deep ‘non-double couple’ earthquake using very broadband data, *Geophys. Res. Lett.*, **17**, 227–230.
- Kuge, K. & Kawakatsu, H., 1992. Significance of non-double couple components of deep and intermediate-depth earthquakes: implications from moment tensor inversions of long-period seismic waves, *Phys. Earth planet. Interiors*, in press.
- Kumazawa, M. & Anderson, O. R., 1969. Elastic moduli, pressure derivatives, and temperature derivatives of single-crystal olivine and single-crystal forsterite, *J. geophys. Res.*, **74**, 5961–5972.
- Masters, G. & Gilbert, F., 1983. Attenuation in the earth at low frequencies, *Phil. Trans. R. Soc. London A*, **308**, 479–522.
- Meade, C. & Jeanloz, R., 1991. Deep-focus earthquakes and recycling of water into the earth’s mantle, *Science*, **252**, 68–72.
- Mikumo, T., 1972. Focal process of deep and intermediate earthquakes around Japan as inferred from long-period *P* and *S* waveforms, *Phys. Earth planet. Interiors*, **6**, 293–299.
- Nábělek, J. L., 1984. Determination of earthquake source parameters from inversion of body waves, *PhD. thesis*, Massachusetts Inst. of Technology, Cambridge, Massachusetts.
- Nábělek, J. L., Chen, W-P. & Ye, H., 1987. The Tangshan earthquake sequence and its implications for the evolution of the North China basin, *J. geophys. res.*, **92**, 12615–12628.
- Oike, K., 1971. On the nature of the occurrence of intermediate and deep earthquakes 3. Focal mechanisms of multiplets, *Bull. Disaster Prevention Res. Inst. Kyoto Univ.*, **21**, 153–178.
- Raleigh, C. B. & Paterson, M. S., 1965. Experimental deformation of serpentinite and its tectonic implications, *J. geophys. Res.*, **70**, 3965–3985.
- Randall, M. J., 1966. Seismic radiation from a sudden phase transition, *J. geophys. Res.*, **71**, 5297–5302.
- Riedesel, M. A. & Jordan, T. H., 1989. Display and assessment of seismic moment tensors, *Bull. seism. Soc. Am.*, **79**, 85–100.
- Satake, K., 1985. Effects of station coverage on moment tensor inversion, *Bull. seism. Soc. Am.*, **75**, 1657–1667.
- Sawamoto, H., Weidner, D. J., Sasaki, S. & Kumazawa, M., 1984. Single-crystal elastic properties of the modified spinel (beta) phase of magnesium orthosilicate, *Science*, **224**, 749–751.
- Solomon, S. C. & Julian, B. R., 1974. Seismic constraints on

- ocean-ridge mantle structure: anomalous fault-plane solutions from first motions, *Geophys. J. R. astr. Soc.*, **38**, 265–285.
- Strelitz, R. A., 1980. The fate of the downgoing slab: a study of the moment tensors from body waves of complex deep-focus earthquakes, *Phys. Earth planet. Interiors*, **21**, 83–96.
- Sung, C. & Burns, R. G., 1976. Kinetics of the olivine → spinel transition: implications to deep-focus earthquake genesis, *Earth planet. Sci. Lett.*, **32**, 165–170.
- Vasco, D. W., 1990. Moment-tensor: searching for non-double couple earthquakes, *Bull. seism. Soc. Am.*, **80**, 354–371.
- Yoshida, Y. & Abe, K., 1992. Source mechanism of the Luzon, Philippines earthquake of July 16, 1990, *Geophys. Res. Lett.*, **19**, 545–548.